5-24-2011

Photoassociative spectroscopy of ultracold metastable argon

M. K. Shaffer
Old Dominion University

G. Ranjit
Old Dominion University

C. I. Sukenik
Old Dominion University

M. Walhout
Calvin University

Photoassociative spectroscopy of ultracold metastable argon

M. K. Shaffer, G. Ranjit, and C. I. Sukenik
Department of Physics, Old Dominion University, Norfolk, Virginia 23529, USA

M. Walhout
Department of Physics and Astronomy, Calvin College, Grand Rapids, Michigan 49546, USA
(Received 28 February 2011; published 24 May 2011)

We present results of photoassociative spectroscopy performed on ultracold metastable argon atoms in a magneto-optical trap. Ion spectra are obtained with laser detuning up to a few gigahertz below the $4s[3/2]_2 \rightarrow 4p[5/2]_3$ trapping transition at 811 nm and with intensities in a range of $\sim(10^2$–$10^5)I_{\mathrm{Sat}}$. We also compute dipole-dipole potentials for both singly and doubly excited diatomic molecules and use a Leroy-Bernstein analysis to determine the approximate vibrational spacings in the $(s + p)$ and $(p + p)$ manifolds. Based on this theoretical framework, we explain a broad background feature in our data and suggest that double-excitation mechanisms are likely responsible for sharp dips in the ion signal.

DOI: 10.1103/PhysRevA.83.052516 PACS number(s): 33.20.−t

I. INTRODUCTION

Photoassociation (PA) is the process by which two initially free atoms absorb one or more photons and form a bound molecule in an excited energy state [1]. If the atomic sample has a narrow thermal distribution, as is typical for trapped clouds at ultracold temperatures, well-resolved resonances in the PA spectrum may reveal vibrational and rotational states within specific diatomic potentials. This effect has been exploited with great success in studies of very long range potentials, most notably those involving the resonant dipole-dipole interaction, which has a C_3/R^3 dependence at large internuclear distance R. A PA spectrum may also exhibit broad features that arise when a system is excited into spatially localized superpositions of energy eigenstates, which tend to be short lived. For photon energies just below the dissociation limit, such features result from a brief period of inward acceleration at the outer reaches of a long-range attractive potential; this dynamical effect increases the inbound flux for "light-assisted collisions." In this paper we present PA spectra for argon and interpret its broad features in terms of single-photon absorption, while attributing certain narrow structures to resonant two-photon transitions.

In our experiment (performed at Old Dominion University), metastable argon (Ar*) atoms are confined in a magneto-optical trap (MOT) and exposed to light from a probe laser beam tuned near the $4s[3/2]_2 \rightarrow 4p[5/2]_3$ trapping transition. PA spectra are obtained as the probe frequency is scanned over a range of several gigahertz and the trap's rate of ion production is monitored. Because the metastable $4s[3/2]_2$ state lies 11.55 eV above the ground state and only ∼4.2 eV below its 15.75-eV ionization energy, Penning ionization ($\mathrm{Ar}^* + \mathrm{Ar}^* \rightarrow \mathrm{Ar} + \mathrm{Ar}^+ + e^-$) and associative ionization ($\mathrm{Ar}^* + \mathrm{Ar}^* \rightarrow \mathrm{Ar}_2^+ + e^-$) represent two highly probable collision mechanisms that can lead to the loss of atoms from the trap. It is known that these processes can be modified significantly when probe light is tuned to the red side of an atomic resonance. As has been demonstrated in studies of other rare gases, the frequency dependence of the ion signal is closely related to the spectrum of bound molecular states [2–4].

One of our goals here is to develop a specific theoretical model that can help explain the main features of our data. Our analysis will take several cues from the theoretical work reported in a recent study of PA in Kr* at Calvin College [3]. In that project, experimental ion and fluorescence signals were obtained simultaneously, and a unified interpretation of the signals was developed. There, the model allowed the probe laser to drive transitions to both the singly excited manifold of $(s + p)$ potentials and the doubly excited manifold of $(p + p)$ or $(s + d)$ potentials. The study focused on the spectroscopic signatures of purely long-range molecular states within each of the manifolds. While such states do not exist for the argon potentials that will concern us here, the dynamical considerations related to single and double excitation will be important as we attempt to explain the main features of our ion spectrum.

II. DIATOMIC POTENTIALS FOR ARGON

The long-range interaction between two metastable-state noble gas atoms was investigated in Ref. [5] while the long-range $(s + p)$ potentials lying above these curves have been calculated in Ref. [6]. To our knowledge, there have been no calculations of doubly excited $(p + p)$ potentials. Most of those potentials would be dominated by C_5/R^5 quadrupole-quadrupole terms, which we can estimate only roughly based on comparisons with coefficients computed for potassium [7]. However, there are cases in which C_5 is zero and the leading term of the potential is C_6/R^6, which arises from the nonresonant dipole-dipole interaction. It is with these cases in mind that we compute the C_6 coefficients for the doubly excited manifold of potentials. This computation is a straightforward extension of the methods of Refs. [3,6], which we use to find C_3 coefficients for the singly excited manifold.

Inputs for our calculation include atomic data (energies and oscillator strengths) for transitions involving 27 different states, which we list in Table I of the Appendix. For those potentials that can be probed with laser light tuned near 811 nm, the $4s[3/2]_2 \rightarrow 4p[5/2]_2$ and $4s[3/2]_2 \rightarrow 4p[5/2]_3$

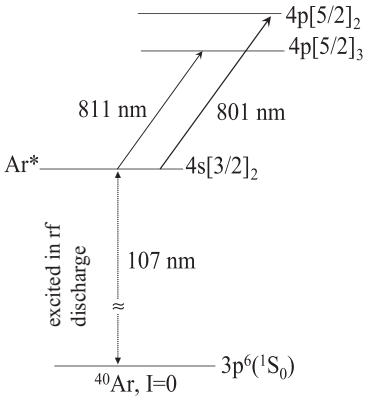

FIG. 1. Some relevant energy levels and transitions in atomic argon.

transitions (Fig. 1) make the largest numerical contributions. Because of the small energy difference between these two transitions, there are large C_3 coefficients for the potentials connected with the $(4s[3/2]_2 + 4p[5/2]_3)$ asymptote. As suggested in Fig. 2(a), it is only for $R \gtrsim 200a_0$ that most of these potentials fall within 10 GHz of the asymptote. However, the figure also shows two singly excited potentials (marked with asterisks) that have much shorter range. These potentials have a spatial dependence closer to that of the doubly excited potentials in Fig. 2(b). We will return to this spatial overlap of potentials in the upper and lower manifolds when we consider the likelihood of double-excitation mechanisms.

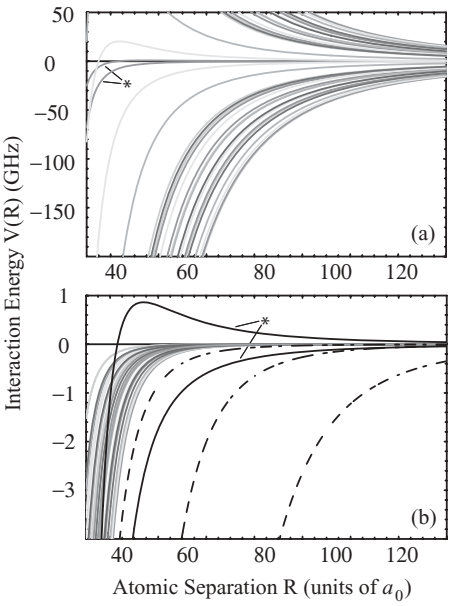

FIG. 2. Potentials associated with the cooling transition in argon. (a) Singly excited potentials connected to the $(4s[3/2]_2 + 4p[5/2]_3)$ asymptote. (b) Singly and doubly excited potentials connected to the $(4s[3/2]_2 + 4p[5/2]_3)$ and $(4p[5/2]_3 + 4p[5/2]_3)$ asymptotes, respectively. An asterisk labels the same two singly excited curves in both (a) and (b). Solid curves represent our calculated dipole-dipole potentials. Dashed lines in (b) are potentials of the form C_5/R^5 with $C_5 = 100$, 1000 and 10 000 a.u., respectively (left to right). Various shades of gray are used to distinguish curves with different values of Ω (which is the projection of total electronic angular momentum onto the internuclear axis). The unit of a_0 is the Bohr radius (0.0529 nm). As mentioned near the end of the paper, large Franck-Condon factors for transitions from the singly to doubly excited curves in (b) may increase the double-excitation rate for $20a_0 < R < 80a_0$.

III. EXPERIMENTAL TECHNIQUE

Argon atoms are excited to the $4s[3/2]_2$ metastable state (our effective ground state) in a radio frequency discharge as described in Ref. [8] and transported to a vacuum chamber, where they are trapped in our MOT. The trapping laser beams are tuned 12 MHz below the atomic resonance at 811 nm. Typically, we have $\sim 1\times10^6$ atoms trapped at densities of $\sim 1\times10^{10}$ atoms/cm^3.

The probe light is generated by a diode laser system that uses a Littman-Metcalf external cavity in a master-slave configuration and has been electronically optimized for long, mode-hop-free frequency scanning [9]. Capable of controlled scans of over 20 GHz, the probe laser can deliver 50 mW of TEM_{00} laser light to the trapped cloud via fiber-optic cable. The probe light can be switched off with an acousto-optical modulator located upstream from the fiber. The beam is focused to a calculated waist size of $\sim$130 μm at the position of the trapped atom cloud, and after emerging from the MOT chamber it is refocused and retroreflected into the sample. We find that addition of the retroreflected beam increases the overall signal size by a factor of roughly 3–5 and is crucial for clearly observing the dips in ionization shown in Figs. 4 and 5. The counterpropagating beams are given orthogonal linear polarizations, so that the polarization in the standing wave field varies dramatically on the scale of a single wavelength. However, the observed spectral features do not appear to depend on the polarization of the retroreflected beam. While retroreflecting the probe beam can set up an optical lattice and give rise to further cooling, we believe that the principal effect of the addition of the retroreflection is to counter the mechanical push of the high-intensity probe beam.

We monitor our frequency scans and obtain frequency calibration data by using an Ar* saturated absorption spectrometer as an absolute reference, a 300-MHz Fabry-Perot spectrum analyzer, and a 10-GHz solid etalon (the thick etalon from a Coherent 899 Ti:sapphire laser). A signal from each of these devices is recorded by a LabView data acquisition program. By using these tools, we maintain an uncertainty of a few megahertz in our absolute frequency scale.

Ions are detected with a channel electron multiplier (Sjuts KBL10RS) located about 3 cm from the MOT. In the absence of probe light, the count rate generated by the MOT alone is $\sim$10–100 kHz. This signal is made up mainly of Ar^+ and Ar_2^+ ions produced primarily in light-assisted s-p collisions [10]. In a previous experiment, we observed these ions using a quadrupole mass spectrometer fashioned from a modified Stanford Research RGA200 residual gas analyzer [8]. To eliminate this large background rate, we turn off the trapping light whenever a pulse of probe light is applied. This procedure gives us a much smaller background count rate of $<$1 kHz from the MOT, which arises from s-s collisions between atoms in the metastable $4s[3/2]_2$ state. It also allows us to avoid complications that might arise if two-color

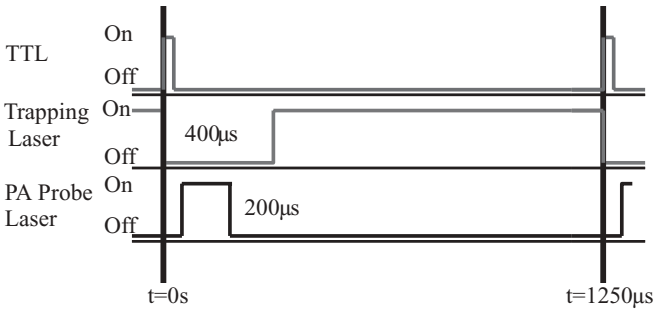

FIG. 3. Timing schematic for photoassociative spectroscopy experiment.

transitions were possible. The background that remains is dominated by a ∼2 kHz rate from the unshuttered atomic beam.

The timing schematic for the experiment is shown in Fig. 3. The switching cycle for each sample starts at $t = 0$. At this time the MOT is fully loaded, except very close to resonance where the probe light greatly disturbs the MOT. The trapping laser is shut off at this instant and remains off for 400 μs. At $t = 30$ μs, the probe laser is switched on and remains on for 200 μs. After $t = 400$ μs the trapping laser is turned on again, allowing the MOT to reload. This sampling cycle occurs every 1.25 ms.

During the 200-μs probe period, one channel of a Stanford Research SR400 photon counter is used to measure the ion rate. The second channel of the photon counter is activated for 200 μs also, but it is delayed 900 μs relative to $t = 0$ and serves to record the background ion signal from the MOT alone. This allows us to characterize the initial MOT conditions at $t = 0$. The SR400 records the total number of ion counts accumulated in each of the two channels over the course of 2000 sampling cycles. The accumulated sum in the background channel allows us to check on the stability of the MOT, while that in the main data channel serves as a single data point in scan plots like those in Figs. 4 and 5. Each of the scans in these figures comprises 2000 data points and requires 5000 s to complete. During each scan, the laser frequency is swept continuously rather than in incremental steps. For the longest scan, each data point is acquired as the frequency

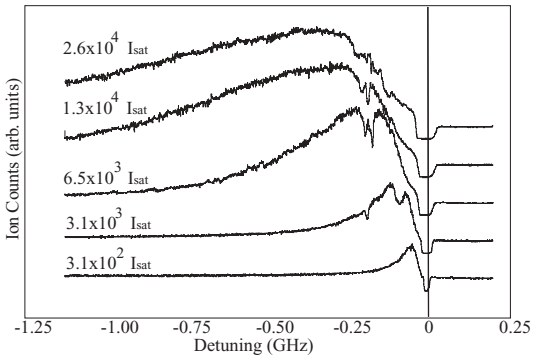

FIG. 4. Photoassociative ionization spectrum for Ar* near the $(4s[3/2]_2 + 4p[5/2]_3)$ asymptote. Spectra are plotted in order of increasing probe intensity starting with the lowest value on the bottom. I_{sat} is the atomic saturation intensity.

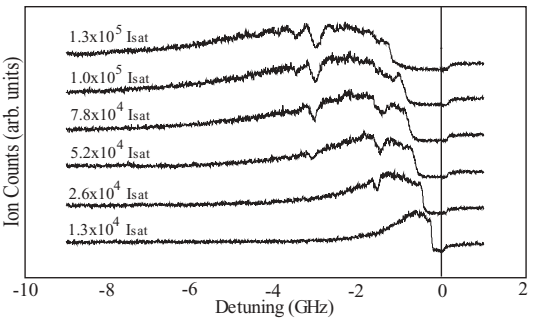

FIG. 5. Photoassociative ionization spectrum for Ar* near the $(4s[3/2]_2 + 4p[5/2]_3)$ asymptote. Spectra are plotted in order of increasing probe intensity starting with the lowest value on the bottom. I_{sat} is the atomic saturation intensity.

sweeps over about 5 MHz, so our frequency resolution is finer than the characteristic widths of the features we observe.

During each probe period, the Zeeman slower light, with an intensity $\sim 30 I_{sat}$ (where the saturation intensity $I_{sat} = 1.44$ mW/cm^2) and tuned 160-MHz red of the trapping transition, remains on and passes directly through the MOT. Having performed tests to show that the dominant features in our ion signal are unaffected by this light, we leave the slower light on in order to maintain the greatest number of atoms in the MOT.

Because the MOT moves slightly from day to day, it is occasionally necessary to tweak the alignment of the probe beam (and its retroreflection) in order to ensure fine overlap with the MOT. This introduces some uncertainty in the exact intensity of the probe beam in the MOT. Direct comparison of probe intensities can be done only when scans are performed without any intermediate beam realignment. The data presented below have been produced so that intensity comparisons within each figure should be valid.

IV. RESULTS

We define the probe detuning as the difference between the probe laser frequency and the natural resonance frequency of the $4s[3/2]_2 \rightarrow 4p[5/2]_3$ transition. To acquire a PA spectrum, we scan the detuning over either a ∼1-GHz or a ∼10-GHz range while cycling through the timing and switching scheme described above. Figures 4 and 5 show ion spectra obtained with different probe intensities, labeled according to the one-way intensity at the MOT. In contrast to the sharp ion *peaks* that have been seen in the He* experiments [2], the distinct resonances in our spectrum appear as *dips* on top of the broad increase in ionization. One goal of our analysis will be to explain why some resonances cause decreases in the ion rate while others cause increases. Another goal will be to account (roughly) for the spacings between the ion dips that we observe. In addition, our explanatory model should provide an understanding of the dynamics underlying the broad background peak, which extends over most of our scanning range and becomes broader as the probe intensity is increased.

We note that higher intensities also produce increased probe-induced distortion (or even destruction) of the MOT when the probe frequency is near the atomic resonance. This degradation of the trap can be attributed to a pair of distinct mechanisms. First, there is the mechanical effect of unbalanced optical forces, which may be non-negligible in our system because of a power mismatch between the counterpropagating probe fields. The forces on individual atoms would be expected to have a frequency dependence that is symmetric about the atomic resonance. However, on the red side of the resonance, where the density of vibrational states is high, near-resonant forces may also be exerted on atomic pairs. Also on this same, red side of the atomic resonance, a second trap-loss mechanism becomes important: the "radiative escape" of atoms occurs when well-separated atoms are excited to long-range attractive $(s + p)$ potentials, gain kinetic energy as they accelerate toward small R, and decay spontaneously into untrapped atomic states. These MOT-degrading effects are evident in our spectra, and they limit our ability to obtain useful information close to the dissociation limit.

V. ANALYSIS AND DISCUSSION OF RESULTS

Here we will first consider the broad background peak and then the resonant dips that are notched into it. We can explain the broad peak in terms of the excitation-and-acceleration mechanism just mentioned. Besides facilitating radiative escape, this mechanism also enhances the probability of ionization. The enhancement can be understood as follows. At large R, a resonant interaction with the probe laser can create superpositions of the closely spaced vibrational states in the long-range, attractive $(s + p)$ potentials in the singly excited manifold. As long as a given pair of atoms lies near the Condon points for these potentials, the resonance condition can be sustained over a range of frequencies, and the pair can undergo Rabi oscillations and occasionally absorb and spontaneously emit photons. The net effect of these interactions is to produce a mixture of $(s + s)$ and $(s + p)$ states in the sample, both of which will have undergone strong inward acceleration (toward $R = 0$) on long-range C_3/R^3 potentials. The probe thus causes an increase in the inward collisional flux and, consequently, an enhancement in the ion count rate. Moreover, since ionization is more likely for s-p collisions than for s-s collisions, the ion rate is additionally augmented by the presence of the $(s + p)$ population. For probe frequencies very close to the atomic resonance, the $(s + p)$ population is produced at extremely large distances and is likely to decay spontaneously before an atom pair reaches the short distance range where ionization occurs. The right side of the broad ion peak slopes downward toward the resonance because of this limiting effect on the $(s + p)$ survival. As seen in each of the graphs, the downward slope gives way to a precipitous drop-off in the ion signal, which can be attributed to the MOT-disturbing effects of mechanical forces and radiative escape, which were described above. For frequencies on the red (left) side of the peak's maximum, the ion rate falls off not because of limited excited-state survival but rather because of limited excited-state production. That is, at large detunings and short distances, the excitation of $(s + p)$ states becomes less and less probable, because the sample's pair-distribution function and the density of vibrational energy states decrease as R gets smaller.

With increasing probe intensity, the background signal grows and broadens, and the position of its maximum value shifts toward larger detuning. These effects can be attributed to a power-broadening effect in the atomic and molecular resonances. The main result of this broadening is an increase in the collisional flux that feeds the overall signal. In addition, the Rabi oscillations that underlie the broadening effect have specific dynamical consequences. For small detunings and large distances, the oscillations produce coherent superpositions of $(s + s)$, $(s + p)$, and $(p + p)$ states. In this situation, survival of the $(s + p)$ component is limited not only by spontaneous emission but also by stimulated transitions into other manifolds. As suggested previously, the $(s + s)$ component contributes a lower ionization rate than the $(s + p)$. The same is likely to be true of the $(p + p)$ component, except that in this case ionization is made even less likely by the competing mechanism of radiative decay, which is roughly twice as probable for $(p + p)$ states as for $(s + p)$ states. These saturation-dependent mechanisms help to limit the $(s + p)$ survival; therefore, they provide an explanation for why the blue side of the background peak becomes less steep and moves toward larger detuning as the probe intensity is increased.

Having explained the broad background peak in our ion data, we can now address the question of why there are pronounced dips in the ion rate relative to the background. We start by listing various kinds of molecular states that are likely to have low ionization rates; in each case, we assess the likelihood that such states are produced in our experiment.

(a) Purely long-range states [11]: These states correspond to vibrational levels in a certain kind of molecular binding potential, for which even the inner, repulsive wall is located at large R. In these systems, the purely long-range potential holds atoms sufficiently far apart that they cannot undergo an ionizing collision. Excitation to such states can provide a way of reducing the ionization rate in a MOT. Such a mechanism has been cited in order to explain PA spectra for He* [12] and Kr* [3]. However, as seen in Fig. 2, there are no purely long-range potentials connected to the $(4s[3/2]_2 + 4p[5/2]_3)$ or $(4p[5/2]_3 + 4p[5/2]_3)$ asymptotes, so this is not a likely explanation for our data. [We note that purely long-range states do exist near other Ar* $(s + p)$ asymptotes, but they are not relevant to the present discussion.]

(b) Spin-polarized states: It is well known that collisional ionization in ultracold He* can be suppressed by way of spin polarization [13], with the suppression calculated to be up to a factor of 10^5 [14]. This effect can be understood in terms of spin conservation and can be important for systems in which spin is a good quantum number. In rare gases other than helium, however, orbital and spin angular momenta are strongly coupled, and the suppression of ionization is much less pronounced in spin-polarized samples. For instance, polarizing atoms in a Ne* MOT reduces the ionization rate by just one or two orders of magnitude [15] and in Xe* the suppression effect appears to be altogether absent [16].

The suppression factor for Ar* is expected to lie somewhere between the Ne and Xe cases, so it seems likely to play at most

a minimal role in our experiment. In any case, the molecular states that we may excite with our probe lie in the $(s + p)$ and the $(p + p)$ manifolds and not the $(s + s)$ manifold that has been the concern of previous work relating to the spin-conservation principle. While there may be some carryover of the principle in the excited manifolds, we assume that any suppression of ionization related to this effect will be negligible in our system.

(c) States with extra nonionizing loss channels: Putting atom pairs into these states introduces a mechanism that competes with ionization and therefore reduces the net rate of ion production in the sample. For example, as mentioned above in the context of limited $(s + p)$ survival, the excitation of $(p + p)$ states opens (or widens) a radiative escape channel that removes some of the collisional flux from the ionization channel. A similar effect was seen in [3] and was used to distinguish between single- and double-excitation of purely long-range states in Kr. In both of these instances, ion signals are attenuated through a double-excitation mechanism that opens the way to radiative escape. We consider it likely that a similar process is behind the resonant dips in our signal.

Both the widths and the relative spacings of the ion dips are suggestive of a double excitation to the $(p + p)$ manifold shown in Fig. 2(b). The widths appear to indicate a resonance condition stricter than that of the $(s + p)$ excitation dynamics described above. The spacings, which fall in the range of a few hundred megahertz to a few gigahertz, are larger than the energy intervals between high-lying vibrational states in the C_3/R^3 potentials in Fig. 2(a) but are consistent with vibrational spacings in the $(p + p)$ potentials. In the following section we outline the analytical procedure leading us to this last conclusion.

A. Leroy-Bernstein analysis

In order to estimate the vibrational energies in our potentials, we first model the long-range dependence of each potential as $V(R) = D - C_n/R^n$, where D is the dissociation energy, n is an integer, and C_n is a constant of the leading term in a multipole expansion. As noted earlier, while in general the leading nonzero long-range term of the $(p + p)$ potential will be C_5/R^5 arising from a quadrupole-quadrupole interaction, we are only able to make a rough estimate of the C_5 coefficient at this time and so we restrict our calculation to the more tractable dipole-dipole interaction. We therefore expect the resonant $(1/R^3)$ form to dominate the $(s + p)$ potential while the nonresonant $(1/R^6)$ form of this interaction will dominate the $(p + p)$ curves when C_5 is zero or small. We find that almost all of the singly excited potentials in Fig. 2, except the two marked with asterisks, can be fit well with C_3/R^3 functions. The C_3 values can be found in Ref. [6]. Meanwhile, C_6/R^6 functions provide good fits for the computed doubly excited potentials, with C_6 values ranging from 200 to 3200 a.u. (see Table II in the Appendix). We note that these coefficients represent fits to our model potentials in which higher-order interactions have been neglected. See Ref. [6] for a discussion of the errors that might be introduced in our method of approximation. Uncertainties from the fitting procedure are at the ∼5% level.

The two singly excited curves marked with asterisks cannot be well approximated in terms of a single power of R, but it is clear that their range is near that of the doubly excited potentials. For the sake of comparison, we note that a very rough C_6/R^6 fit to the monotonic curve produces a C_6 of 7200 a.u.

Because our spectra were taken for high-lying rovibrational levels very near the dissociation limit, we can use the Leroy-Bernstein method to help analyze our results [17]. In this near dissociation technique, where the potential curves are approximated by $V(R)$ above, the locations of the vibrational energy levels are given by

$$E(v) = D - \left[\sqrt{\frac{\pi}{2\mu}}\frac{\Gamma\left(1+\frac{1}{n}\right)}{\Gamma\left(\frac{1}{2}+\frac{1}{n}\right)}\frac{\hbar(n-2)}{C_n^{1/n}}(v_D - v)\right]^{\frac{2n}{n-2}}, \quad (1)$$

where D is the molecular dissociation energy, $E(v)$ is the energy of the vibrational level v, v_D is the effective noninteger vibrational index at the dissociation level, n is the order of the leading coefficient for the molecular potential, μ is the reduced mass, and Γ is the Gamma function.

If the energy spacings in a vibrational series can be identified from an experimental spectrum, the expression above can be used to find C_n and v_D. This is not, however, the case here. In our data, there are only a few resonance peaks in a region where there is considerable overlap of resonances from different potentials, and we are unable to identify distinct spectral series. Nevertheless, we can gain insight from the Leroy-Bernstein formula by inserting our calculated and estimated coefficients and noting the energy spacings for vibrational levels close to the dissociation limit, where our data were obtained. Using our calculated C_n coefficients and Eq. (1), we can calculate a value of $(v_D - v)$ which corresponds to the location of the observed peaks. When we do this we find that for all but two of the potentials, if the observed peaks were to originate from the singly excited $(4s[3/2]_2 + 4p[5/2]_3)$ manifold, the corresponding values for $(v_D - v)$ would span ∼15 to 40, with no obvious pattern. For the two shorter-range potentials, the $(v_D - v)$ values range from 6.9 to 13.5 in one case and 3.0 to 5.9 in the other. On the other hand, for doubly excited potentials with C_6/R^6 character, we find $(v_D - v)$ ranging from 0.4 to 2.4. Furthermore, if we assume that C_5 is not negligible, we can use the potassium model to provide an estimated C_5 for argon between 100 and 3000 a.u., in which case $(v_D - v)$ falls between 1 and 6. We speculate that it is likely that a detailed calculation of doubly excited potentials will show that some of the potentials will be dominated by a C_5 term and others by a C_6 term. While this analysis does not exclude the possibility that the observed resonances arise from excitations to singly excited state potentials, it is clear that the vibrational level spacings of the doubly excited potentials, whether dominated by the quadrupole-quadrupole or dipole-dipole interaction (or a mix of the two), are far more consistent with the spacing of the prominent features observed in our data than those of the singly excited potentials.

B. Additional roles for singly and doubly excited potentials

Given the preceding analysis of vibrational spacings, we think it likely that our ion dips originate in the excitation of

atom pairs to some of the potentials represented in Fig. 2(b). Here we discuss the different roles that might be played by the singly and doubly excited potentials shown in this figure. As mentioned in our discussion of the broad background peak, we can assume that the total collisional flux for an atom pair mainly involves $(s + s)$, $(s + p)$, and $(p + p)$ components. Extending that discussion, we take it that the $(s + p)$ component is normally the primary source of ionization, while transitions to the $(s + s)$ and $(p + p)$ manifolds have the effect of decreasing the ion signal. According to the standard account of the broad background, while the ion signal decreases gradually over this frequency range as a result of a decreasing probability of $(s + p)$ excitation, the $(s + p)$ survival probability remains high. We suggest that ion dips could appear when resonant $(s + p) \rightarrow (p + p)$ transitions compromise this survival probability. Such transitions attenuate the ion signal both by lowering the $(s + p)$ flux and by enhancing the probability of radiative escape. Alternatively, instead of this two-step process, it may be possible that radiative escape alone is enhanced through a doubly resonant two-photon transition of the form $(s + s) \rightarrow (s + p) \rightarrow (p + p)$. The probability for this transition could be appreciable if there are good spatial overlaps (large Franck-Condon factors) for vibrational wave functions in the singly and doubly excited potentials of Fig. 2(b). Evidence for this kind of an effect was discussed in Ref. [3].

For completeness, we also consider the possibility that the dips are the result of transitions from $(s + s)$ potentials to the $(s + p)$ potentials marked with asterisks in Fig. 2. Our Leroy-Bernstein analysis suggests that these transitions would have spacings close to those we observe. However, at present we have no reason to believe that populating the singly excited potentials alone could attenuate the overall rate of ionization. Indeed, if such a reason were to surface, it would seem likely to force a revision of familiar models like the one we have used to explain our background peak.

VI. CONCLUSION

In this paper we have noted the presence of significant features in the photoassociation spectra of ultracold Ar* for laser detuning several gigahertz below the $4s[3/2]_2 \rightarrow 4p[5/2]_3$ trapping transition at 811 nm. Guided by calculations and estimates of the long-range singly and doubly excited state potentials and a Leroy-Bernstein near-dissociation analysis, we have pointed to some possible explanations of how they are produced. While leaving some uncertainty as to the precise causes for the ion dips in the spectrum, we have proposed a pair of likely mechanisms that involve the excitation of doubly excited states. In concluding, we suggest that these mechanisms could be confirmed (and perhaps distinguished) if the radiative escape channel were monitored along with the ionization channel. In Ref. [3], the tradeoff between count rates for ions and ultraviolet photons proved decisive for the identification of double-excitation resonances in purely long-range krypton molecules. In principle, similar information could be obtained for PA dynamics in the argon system. Moreover, information about specific transitions and potentials could be obtained if experiments were done in spin-polarized samples. Such work would provide further tests of the mechanisms proposed here and would contribute to the general understanding of photoassociation in rare gases.

ACKNOWLEDGMENTS

C.I.S. thanks Edgar Vredenbregt for supplying the codes used for the calculations in Ref. [6]. We gratefully acknowledge support from the National Science Foundation (RUI-PHY-0554807 and PHY-0855290), Calvin College, and Old Dominion University.

APPENDIX

Our calculations of the potentials shown in Fig. 2 employs a basis of 27 atomic states, which are listed in Table I. The energies of the states and all of the relevant transition rates (not shown) are taken from Ref. [18]. In converting energy units, we assume 1 cm^{-1} = 29.979 2458 GHz.

The C_6 coefficients for doubly excited states are listed in Table II.

TABLE I. Atomic states that are included as elements of the algebraic basis for computations of the dipole-dipole potentials shown in Fig. 2.

Atomic state (pair-coupling notation)	Energy (cm^{-1})
$4s[3/2]_2$	93 143.76
$4s[3/2]_1$	93 750.5978
$4s'[1/2]_0$	94 553.6652
$4s'[1/2]_1$	95 399.8276
$4p[1/2]_1$	104 102.0990
$4p[1/2]_0$	107 054.2720
$4p[5/2]_3$	105 462.7596
$4p[5/2]_2$	105 617.2700
$4p[3/2]_1$	106 087.2598
$4p[3/2]_2$	106 237.5518
$4p'[3/2]_1$	107 131.7086
$4p'[3/2]_2$	107 289.7001
$4p'[1/2]_1$	107 496.4166
$4p'[1/2]_0$	108 722.6194
$4d[7/2]_4$	119 023.648
$4d[1/2]_1$	118 651.3950
$4d[7/2]_3$	119 212.87
$4d[3/2]_2$	118 906.6110
$4d[3/2]_1$	119 847.77
$4d[5/2]_2$	119 444.83
$4d[5/2]_3$	119 566.03
$6s[3/2]_2$	119 683.0821
$6s[3/2]_1$	119 760.1725
$3d[3/2]_1$	114 147.732
$4d[1/2]_0$	118 512.197
$5s'[1/2]_0$	114 861.635
$5s'[1/2]_1$	114 975.019

TABLE II. C_6 coefficients for doubly excited states. Ω is the projection of total angular momentum onto the internuclear axis of the dimer molecule.

Ω	C_6 (hartree a_o^6)
0	3149
0	1949
0	1251
0	790
0	741
0	190
0	190
1	3089
1	1884
1	1154
1	857
1	363
1	362
2	2618
2	1556
2	893
2	430
2	375
3	2432
3	1273
3	561
3	308
4	2077
4	903
4	289
5	1655
5	515
6	1250

[1] K. M. Jones, E. Tiesinga, P. D. Lett, and P. S. Julienne, Rev. Mod. Phys. **78**, 483 (2006).

[2] N. Herschbach, P. J. J. Tol, W. Vassen, W. Hogervorst, G. Woestenenk, J. W. Thomsen, P. van der Straten, and A. Niehaus, Phys. Rev. Lett. **84**, 1874 (2000).

[3] Z. S. Smith, A. Harmon, J. Banister, R. Norman, K. Hoogeboom-Pot, and M. Walhout, Phys. Rev. A **81**, 013407 (2010).

[4] J. Leonard, A. P. Mosk, M. Walhout, P. van der Straten, M. Leduc, and C. Cohen-Tannoudji, Phys. Rev. A **69**, 032702 (2004).

[5] A. Derevianko and A. Dalgarno, Phys. Rev. A **62**, 062501 (2000).

[6] M. R. Doery, E. J. D. Vredenbregt, J. G. C. Tempelaars, H. C. W. Beijerinck, and B. J. Verhaar, Phys. Rev. A **57**, 3603 (1998).

[7] M. Marinescu, Phys. Rev. A **56**, 4764 (1997).

[8] H. C. Busch, M. K. Shaffer, E. M. Ahmed, and C. I. Sukenik, Phys. Rev. A **73**, 023406 (2006).

[9] M. K. Shaffer, G. Ranjit, and C. I. Sukenik, Rev. Sci. Instrum. **79**, 046102 (2008).

[10] K.-A. Suominen, K. Burnett, P. S. Julienne, M. Walhout, U. Sterr, C. Orzel, M. Hoogerland, and S. L. Rolston, Phys. Rev. A **53**, 1678 (1996).

[11] W. C. Stwalley, Y.-H. Uang, and G. Pichler, Phys. Rev. Lett. **41**, 1164 (1978).

[12] G. R. Woestenenk, Ph.D. dissertation, Universiteit Utrecht, 2001.

[13] N. Herschbach, P. J. J. Tol, W. Hogervorst, and W. Vassen, Phys. Rev. A **61**, 050702(R) (2000).

[14] P. O. Fedichev, M. W. Reynolds, U. M. Rahmanov, and G. V. Shlyapnikov, Phys. Rev. A **53**, 1447 (1996).

[15] P. Spoden, M. Zinner, N. Herschbach, W. J. van Drunen, W. Ertmer, and G. Birkl, Phys. Rev. Lett. **94**, 223201 (2005).

[16] C. Orzel, M. Walhout, U. Sterr, P. S. Julienne, and S. L. Rolston, Phys. Rev. A **59**, 1926 (1999).

[17] R. J. LeRoy and R. B. Bernstein, J. Chem. Phys. **52**, 3869 (1970).

[18] Y. Ralchenko, A. E. Kramida, J. Reader, and NIST ASD Team, NIST Atomic Spectra Database (ver. 4.0.1), [http://physics.nist.gov/asd] [2011, January 3].